https://doi.org/10.5194/essd-2025-284
Preprint. Discussion started: 24 June 2025
© Author(s) 2025. CC BY 4.0 License.

Open Access Earth System Science Data Discussions

In-situ aerosol measurements at the Arctic Sammaltunturi measurement station during the Pallas Cloud Experiment 2022

John Backman[1], Krista Luoma[1], Henri Servomaa[1], Ville Vakkari[1], and David Brus[1]
[1]Atmospheric Composition Research, Finnish Meteorological Institute, Helsinki, Finland
Correspondence: john.backman@fmi.fi

Abstract.

This work describes the in-situ aerosol measurements at the Arctic Sammaltunturi measurement station in Pallas in northern Finland. This data paper, describes the instruments and the data post processing of key aerosol particle measurements that are relevant for cloud properties. Data reported here are part of the Pallas Cloud Experiment in 2022 (PaCE2022). The in-situ measurements described in this paper and are complementary to the research related to the PaCE 2022 campaign that investigates aerosol and cloud properties such as transects and profiles obtained from balloons, drones, and remote sensing techniques. All data from the campaign resides in a campaign dedicated data repository for easy access and overview. In addition, this data paper will also act as a future reference on how aerosol measurements are conducted and post-processed at the site for future publications. The data set is available at PaCE 2022 campaign data repository at https://zenodo.org/communities/pace2022/ (last access: May 7, 2025). The data described here is available at https://doi.org/10.5281/zenodo.14900651 (last access: May 7, 2025) (Backman et al., 2025).

1 Background

Aerosol particles and clouds are an intricate part of the climate system (IPCC, 2023). Aerosol particle suspended in air interact directly with solar radiation by scattering and/or absorbing solar radiation. How much aerosol particles interact with the sun's radiation directly depends on the optical properties of the aerosol particles and the albedo of the underlying surface (Haywood and Shine, 1995). Aerosol particles can also act as cloud condensation nuclei (CCN) or ice nuclei (IN) onto which water vapor can condense to form cloud droplets or ice crystals. The ability of an aerosol particle to form cloud droplets is influenced mainly by aerosol particle size, and to a lesser extent the aerosol particles chemical composition (e.g. Dusek et al. (2006) REF?). The number concentration of aerosol particles that can act as CCN is also of vital importance. An abundance of CCN active aerosol particles will form cloud droplets that are smaller in size which makes for brighter clouds, given that the amount of condensable water vapor stays the same (Twomey, 1974, 1977). Moreover, brighter clouds with smaller cloud droplets are less prone to form precipitation (Albrecht, 1989; Dagan et al., 2023). These aerosol-cloud interactions (ACI) are important for the Earth's climate as water vapor and clouds are way more important for the Earth's radiation budget than any non-condensable greenhouse gas.

The Arctic is a particularly vulnerable when it comes to climate change. Research has shown that the Arctic is warming four times faster than the rest of the world (Rantanen et al., 2022). Snow and sea ice are the most reflective surfaces that occur

https://doi.org/10.5194/essd-2025-284
Preprint. Discussion started: 24 June 2025
© Author(s) 2025. CC BY 4.0 License.

naturally on Earth. These bright surfaces are able to reflect the sun's energy back into space, thus cooling the climate. Open water, on the other hand, is the most absorbing surface that occurs naturally on Earth. In the warming Arctic, snow and sea ice is replaced by open water, a highly reflective surface is replaced by a highly absorbing one, thus converting more of the sun's energy into heat. This phenomenon is known as Arctic amplification and is the reason that the Arctic is warming at such a fast rate (Serreze et al., 2009). The implications of these rapid changes currently happening in Arctic on aerosol and low-level clouds have remained elusive.

Current aerosol modeling efforts reported the inherent limitations in deriving vertical aerosol distributions solely from surface-based measurements. As highlighted by Morrison et al. (2022), the vertical stratification of aerosols within the atmospheric column, particularly their relative positioning with respect to cloud layers, can have a significant impact on the sign of the radiative forcing, potentially inverting its sign. Also, large-scale climate models struggle simulating low-level Arctic mixed-phase clouds. A significant contributing factor to these discrepancies lies in the incomplete representation of aerosol microphysical properties, specifically those that could act as cloud condensation nuclei (CCN) and ice nucleating particles (INP). Under specific thermodynamic regimes prevalent in the Arctic, those factors were found to be limiting for cloud formation processes (Schmale et al., 2021).

In the last two decades, extensive work has been done on ACI during Pallas Cloud Experiments (PaCE). Our previous research has shown that even the relatively clean air in Finnish subarctic is a complex mixture of potential aerosol precursors from various marine, biological and anthropogenic sources and that changes in anthropogenic emissions can have an impact on subarctic aerosol up to CCN sizes and also cloud micro-physical properties (e.g. Komppula et al., 2005; Kivekäs et al., 2009; Lihavainen et al., 2010; Asmi et al., 2011; Anttila et al., 2012; Filioglou et al., 2017; Gérard et al., 2019; Doulgeris et al., 2020, 2023). This paper is a data description paper for the in-situ aerosol measurements conducted during the Pallas Cloud Experiment (PaCE) in 2022 at Pallas measurement site in Northern Finland. This data is complementary to other data produced during the measurement campaign that includes vertical profiles and transects of a wide range of in-situ aerosol, cloud and remote sensing measurements, carried out on wide range of platforms including tethered balloons, drones, and UAVs. The duration of the PaCE 2022 campaign was from 15 September 2022 to 15 December 2022. An overview of the PaCE 2022 campaign is provided by Brus et al. (2025).

2 Instrumentation

2.1 Measurement location and inlets

Here we present the key physical aerosol particle parameters measured continuously at the Pallas Sammaltunturi measurements station (elevation 565 m a.m.s.l.). The station is located on top of a fell and is located at 67.97361°N 24.11583°E in the municipality of Muonio in the Lappland region in northern Finland (Hatakka et al., 2003). Due to the altitude of the station, the station is occasionally inside clouds in the fall and early winter.

A summary table of the instruments, the inlets they are connected to, and the means by which the sample aerosol is dried, is summarized in Table 1 and the inlets are shown in Fig. 1.

https://doi.org/10.5194/essd-2025-284
Preprint. Discussion started: 24 June 2025
© Author(s) 2025. CC BY 4.0 License.

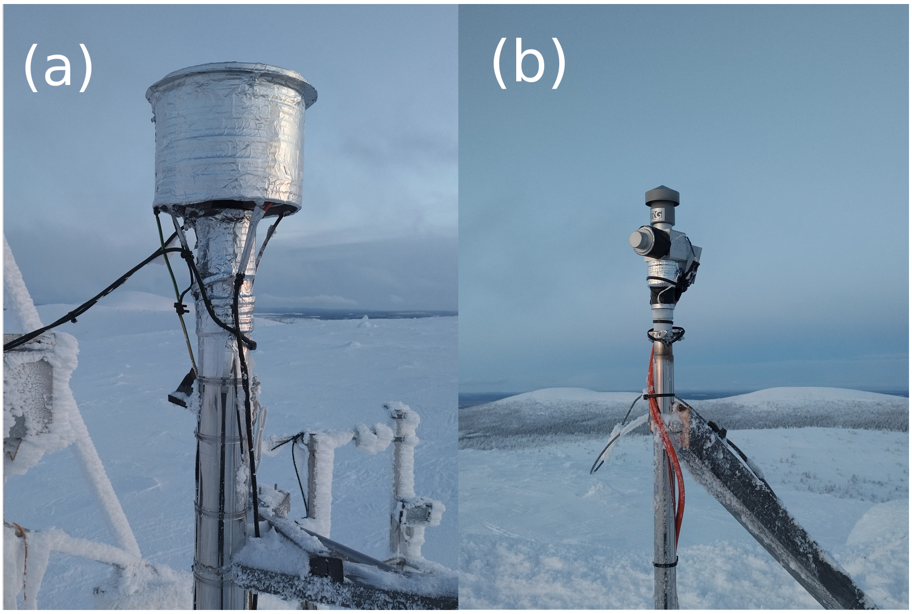

Figure 1. Pictures of the total inlet (a) and the $PM_{2.5}$ inlet (b).

The in-situ aerosol instruments at the Sammaltunturi station are measuring through two aerosol inlets: a total inlet with no cut-off, and an inlet with a cut-off of 2.5 µm. The inlets are located 2 m above the station's roof and about 6 m above ground. Both inlets are heated to avoid snow and ice buildup when the station is inside clouds or when it is snowing.

The total aerosol inlet is a custom built inlet and based on the design that was first deployed to the Jungfraujoch station in Switzerland (Weingartner et al., 1999). The design of Jungfraujoch inlet was received through personal communication and replicated at the Finnish Meteorological Institute's workshop. The inlet is essentially a big hood. The sample air is drawn from within the hood and down into the station through the roof. In addition to the inlet, the sample tube is also actively temperature controlled so that the sample air warms up before reaching the inside of the measurement station.

The second inlet is a total suspended particle (TSP) inlet by URG Corp. (USA). Downstream of the TSP inlet is a $PM_{2.5}$ cyclone (MesaLabs BGI $PM_{2.5}$ Sharp Cut Cyclone) which is also heated so that the cyclone won't get clogged by snow or ice.

After the inlets, in both of the measurement lines, the sample air is dried with a Naphion dryer (Permapure Monotube Dryer MD-700-24S) and dry compressed air. The Naphion dryers are 60 cm long with a tube diameter of 17 mm. The dryers are located inside the measurement hut. The diffusional losses of the 60 cm long Nafion driers have been characterized to have an equivalent length of 2.5 m of conductive tubing when accounting for diffusional losses (Dick et al., 1995). The Nafion tubes are installed vertically under the inlets to avoid losses due to gravitational settling. The moisture permiates through the Naphion membrane from the sample air is flushed away with dry compressed air which is flowing in the opposite direction of the sample air. This configuration maximizes the efficiency of the drier. The dew point of the compressed air is about -40 °C. The temperature (T) and relative humidity (RH) of the sample air, in both inlets, are monitored with Vaisala HMP110 sensors.

https://doi.org/10.5194/essd-2025-284
Preprint. Discussion started: 24 June 2025
© Author(s) 2025. CC BY 4.0 License.

Table 1. Summary of the instruments with information on their inlet, drying method, their native time resolution (Δt), and last participation on ECAC inter-comparison workshops.

Instrument	Inlet	Dryer	Δt	ECAC
CPC (3772)	PM2.5	Naphion	1 s	no
DMPS	PM2.5	Naphion	6.5 min	2021
CCN	PM2.5	Naphion	1 s	no
MAAP	PM2.5	Naphion	1 s	2017
APS	Total	Naphion	1 min	no
AE-33	Total	Naphion	1 min	2019, 2023
Nephelometer	Total	Naphion	5 min	2017, 2023

In addition to the aerosol instruments, a Vaisala visibility sensor (model FD12P) is used to check if the station is inside clouds, or not. The visibility sensor is also mounted on the roof of the measurement building. In this work, the station is considered to be inside a cloud if the visibility is below 1 km. The data has been flagged accordingly.

2.2 In-situ instruments

The Pallas Sammaltunturi measurement station is part of the pan-European network for Aerosols, Clouds, and Trace Gases Research Infrastructure (ACTRIS) network, which provides funding, technical support, calibration and quality assurance through inter-comparison workshops, through the European Center for Aerosol Calibration and Characterization (ECAC). Not all instruments at the station are part of the ACTRIS network, but those who are have participated in the ECAC workshops either before or after the PaCE 2022 campaign.

2.2.1 CPC

Total particle number concentrations (PNC) are measured with condensation particle counters (CPCs). At Pallas, the CPCs use buthanol as a working fluid. Butanol is used to increase the size of the particles for subsequent detection by optical means. The CPCs are laminar flow CPCs where all the sample aerosol flows through a warm saturation chamber, which saturates the sample air with butanol vapor. The sample is then cooled in a diffusion-type cooling section where the aerosol particles grow by condensation to optically detectable sizes. The growth through condensation is achieved by super-saturation of the butanol vapor in the cooling section. An overview of the development of these kinds of CPCs and their detailed working principles is given by McMurry (2000). The CPC to measure total particle number concentrations at Pallas after the PM2.5 inlet is a TSI Inc. model 3772 buthanol CPC (Hermann et al., 2007). The 3772 CPC's 50% cutoff diameter is around 7 nm with the standard operating parameters (Tuch et al., 2016), namely the temperature difference between the saturator and the condenser.

https://doi.org/10.5194/essd-2025-284
Preprint. Discussion started: 24 June 2025
© Author(s) 2025. CC BY 4.0 License.

2.2.2 DMPS

Particle number size distributions (PNSD) are measured with custom built Differential Mobility Particle Analyzers (DMPS). The aerosol particles are selected using a Vienna-type Differential Mobiliy Analyzer (DMA, Winklmayr et al. (1991)) and PNC after the DMA is measured with a CPC (TSI Inc. model 3010). In the DMA, particles are selected by their electrical mobility in an electrical field as they flow through the DMA, Knutson and Whitby (1975). Since the DMA measures electrical mobility, the particles need to have a charge. Hence, before the DMA, a Ni-63 radioactive source is used as a neutralizer and charger to achieve a known charge distribution of the aerosol (Wiedensohler, 1988). A known charge distribution is achieved using a bipolar charger of Ni-63 with an initial activity of 370 MBq. The probability of charged particles to pass through the DMA's electric field is described by the DMA's transfer function, e.g. Zhang and Flagan (1996). The transfer function, without considering diffusion, is a function of the flow rates through the DMA, Flagan (1999). The flow rates have been chosen so that the aerosol-to-sheath flow rate has a ratio of 1/5 which give a broad transfer function, but allows for the detection of particles up to 800 nm in size. The smallest size of the DMPS is 10 nm.

2.2.3 CCN

The Cloud Condensation Nuclei (CCN) were measured with a continuous-flow streamwise thermal-gradient CCN counter (CCNc-100, e.g. Rose et al. (2008)), manufactured by Droplet Measurement Technologies, Inc. (DMT). The CCNc-100 operates on the principle of creating a supersaturated environment to CCN into droplets. The core of the instrument is a continuous-flow thermal-gradient diffusion chamber, where a controlled temperature gradient is established. Since water vapor diffuses faster than heat, the temperature gradient results in a supersaturated environment inside. Aerosol particles are drawn into the chamber where they activate at the preset level of supersaturation uptake water vapor and grow into droplets. At the bottom of the chamber is an optical particle counter (OPC) that is used to determine the size and number of the droplets by intensity of light scattering (Droplet Measurement Technologies, Manual for Single-Column CCNs, DOC-0086 Revision M, 2017).

The CCNc was connected to the total inlet to be able to sample also dried cloud activated aerosol during the station in-cloud periods. The CCNc setup utilized a three-way valve that allowed switching between total and size resolved sampling of aerosol by CCNc-DMA . In parallel to CCNc and after CCNc-DMA, the total particle number concentration was measured with CPC (model 3010, TSI Inc.). Similarly as above, the CCNc-DMA setup used a bipolar charger of Ni-63.

2.2.4 APS

An aerodoynamic particle sizer (APS) measures the aerosol size distribution in the size range of 0.5 - 20.5 µm based on the aerodynamic diameters of the particles (B. T. Chen and Yeh, 1985). Therefore, the APS size range covers the coarse mode particles, which are typically classified as particles bigger than 1 µm in diameter. Due to their size, the coarse mode particles, although small by numbers, can contribute substantially to total particle mass (PM), and aerosol optical properties.

The basic operating principle of the APS is to measure the time-of-flight of individual particles in an accelerating air flow. The aerosol particle sample is accelerated in a nozzle and the time-of-flight of the particles in the flow are detected by two

https://doi.org/10.5194/essd-2025-284
Preprint. Discussion started: 24 June 2025
© Author(s) 2025. CC BY 4.0 License.

laser beams. Due to their inertia, the aerosol particles do not accelerate as quickly as the air flow, and the time-of-flight of the particles differs between particles because of their mass, shape, density and size. The aerodynamic diameter is defined as the diameter of a spherical particle with a density of 1000 kg m^{-3} that has the same settling velocity as the particle in question. The time-of-flight data of the individual particles are converted to the aerodynamic diameter based on a calibration with polystyrene latex spheres that have known size and density.

For the APS to successfully measure the time-of-flight of an individual particle, the particle has to pass both of the lasers beams and cause two a large enough signals within a certain time window. Invalid measurements are caused by too large particles, particles detected by only one of the laser beams, and by particle coincidence in the measurement volume.

Instrument specific uncertainties and unit-to-unit variability are caused by inaccurate sample and sheath flow rate, the alignment of the flow and the lasers, and impurities in the optics cause uncertainties and unit-to-unit variability. Pfeifer et al. (2016) reported that the unit-to-unit variability of 15 APS instruments is about 10-20 % for particles sized 0.9-3 µm. For smaller and larger particles the variation increases considerably and they recommended to use caution when applying data below 0.9 µm or above 3 µm. Another study by Vasilatou et al. (2022) reported high counting efficiencies between 0.7-5 µm, but it included only a few instruments in the comparison.

2.2.5 Nephelometer

An integrating nephelometer measures the light-scattering coefficient (σ_{sp}) that describes the amount of scattered light over a unit path length. The σ_{sp} is reported in units of Mm^{-1}. At Pallas, the Nephelometer is a TSI Inc. model 3563 Nephelometer (Anderson et al., 1996) measuring at three wavelengths (450, 550, and 700 nm). A review on the development of integrating nephelometers to measure light scattering by aerosol particles is provided by Heintzenberg and Charlson (1996). In brief, the working principle of an integrating nephelometer is that sample air is drawn into a detection chamber where it is illuminated. The illumination is done through a diffusor glass who's surface is perpendicular to the surface of the detector. This geometry provides a cosine weighted illumination of the sensing volume which is desired to derive the σ_{sp} (Eq. 2.3. in Heintzenberg and Charlson (1996)). By shadowing the part of the measurement cell that represents forward scattering angles (< 90°), the integrating nephelometer can detect separately the light that is scattered in backward direction that is described by the hemispheric backscattering coefficient (σ_{bsp}). However, due to the instrument geometry the instrument can not detect light scattering at angles close to 0° and 180° and, therefore, a so-called truncation correction is applied to the data (Anderson and Ogren, 1998). Furthermore, the detection chamber itself must scatter as little light as possible and is hence matte black and should be kept clean from deposited debris.

In practice, the integrating nephelometer measures light-scattering by both the air molecules and the aerosol particles. To obtain the amount of scattering by the aerosol particles alone, the amount of scattering by gases is subtracted from the measurements of sample air. This subtraction is possible by regularly measuring particle free air. To calibrate the instrument, the measurement chamber is filled with a calibrating gas with well-known scattering characteristics (e.g., CO_2). Because light scattering depends on the wavelength (λ), the measurements are optimally conducted at several wavelengths either by using discrete light sources or detectors.

© Author(s) 2025. CC BY 4.0 License.

2.2.6 MAAP

The Multi-Angle absorption photometer (MAAP, Thermo Sci. model 5012) is a filter-based light absorption photometer. Filter based absopriton photometers measure the change in optical properties of the filter tape as aerosol particles deposit onto the filter. The MAAP has three detectors that are used to derive the light absorption coefficient (σ_{ap}) of the aerosol. The σ_{ap} is calculated from the change in the filter properties during a time window of Δt. One detector is used to measure the transmittance of light through the filter, whereas the two other detectors are used to measure the back-scattered light from the filter at multiple (two) angles (Petzold and Schönlinner, 2004; Petzold et al., 2005). The filter transmittance (Tr) is defined as I/I_0 where I is the intensity of light transmitted through the filter and I_0 is the light intensity transmitted through a pristine filter. The back-scattering measurements of the filter is the used in a radiative transfer model to distinguish between diffusely and Gaussian scattered light in the backward direction.

In the MAAP, the Tr and back-scatter measurements are used to account for nonlinearities in the instrument's response as the filter gets laden with aerosol particles. The nonlinearities are compensated for by solving a radiative transfer model using the measurements made on the filter (Petzold and Schönlinner, 2004). The MAAP is a one wavelength instrument and reports equivalent black carbon (eBC, Petzold et al. (2013)) at a wavelength of 637 nm (Müller et al., 2011). The measured σ_{ap} values are converted into eBC mass concentrations using a fixed mass absorption cross section (MAC).

2.2.7 AE-33

The Aethalometer (model AE-33, Magee Scientific) is also a filter-based absorption photometer. The AE-33 derives σ_{ap} from changes in Tr during the time Δt as aerosols are deposited onto the filter on two sample spot areas. The two spots are used to compensate for the nonlinearities in the instruments response as aerosol particles are deposited onto the filter. In the AE-33, a light source illuminates one side of the filter while the detectors are on the other side of the filter measuring the Tr of both sample spots simultaneously. In the AE-33, the Tr measurements are reported as filter attenuation (ATN) values as

$$ATN = -100\, ln\left(\frac{I}{I_0}\right). \tag{1}$$

In the equation above, I/I_0 is the same as Tr. The ATN values are calculated separately for both sample spots, spot 1 and spot 2. The factor of 100 applied for numerical convenience.

As the two spots on the fiber-filter get laden with light absorbing aerosol particles, ATN values increase; i.e. less light reaches the two detector on the opposite side of the light source. The AE-33's dual spot correction algorithm compensates for the non-linearity in the attenuation decrease as particles deposit onto the filter by comparing the change in ATN between the two spots. In brief, this is possible since the flow rate of the two spots are different which means that the accumulation of aerosol particles onto the two different spots differ (Drinovec et al., 2015). The different rate of change in ATN for these two spots, for concurrent measurements, is used to calculate the light absorption coefficient without the non-linear filter loading effects. One additional spot, which does not get loaded with aerosol particles, is used to monitor the intensity of the light source and is not affected by the sample aerosol and is called the reference spot.

https://doi.org/10.5194/essd-2025-284
Preprint. Discussion started: 24 June 2025
© Author(s) 2025. CC BY 4.0 License.

The AE-33 operates at 7 different wavelengths (370, 470, 520, 590, 660, 880 and 950 nm). Similar to the MAAP, σ_{ap} measurements are also reported as eBC mass concentrations by the AE-33 firmware using fixed MAC values. Regular 'zero-flow' and optical tests are automatically run to account for any changes in detector response or light source intensity. When the filter loading has reached a attenuation (ATN) value of 120, the Aethalometer invokes a filter change.

3 Data processing

In the data set, data is reported in UTC 0 h as daily files starting at midnight. All data reported has been converted to standard temperature (T) and pressure (p), which is 273.15 K and 101.325 kPa, henceforth referred to as STP conditions, except the CCN data which is in ambient condition. Although the data is reported at STP conditions, the flow rates (Q) reported for the instruments in this section can be in either STP conditions in liters per minute (lpm) or at ambient conditions as volumetric liters per minute (vlpm). All data with a relative humidity (RH) above 40% has been removed, except for the CPCs measuring total PNC. The RH data as measured in the sample air in the total and $\mathrm{PM}_{2.5}$ inlet is included in the data files so that the user can omit those data afterwards if desired. Furthermore, when the visibility at the station is below 1 km, a flag has been added to the data to show that the station was inside a cloud.

The data is quality assured and corrected for known measurement artifacts while keeping the original time resolution. Invalid measurements (e.g., periods of maintenance or malfunctions) are omitted from the data. The flow rates of the instruments are measured periodically, during site maintenance and is recorded in the station's logbook (not shown).

The sample flow rate of the instruments can directly affect the measurements and the concentrations they report. This holds true for the MAAP, AE-33, CPC, DMPS's CPC, and APS. For these instruments, a flow correction factor F_{flow} has been applied as follows

$$F_{\mathrm{flow}} = \frac{Q_{\mathrm{inst}}}{Q_{\mathrm{meas}}} \qquad (2)$$

where Q_{inst} is the flow rate that the instrument thinks it is measuring with, and Q_{meas} is the measured flow rate that is periodically measured with an external and high-accuracy bubble-flow meter at the inlet port of the instrument. F_{flow} is then the factor by which the concentrations will be multiplied with to get the true concentration.

The naming convention is described by Brus et al. (2025). In brief, all data described in this work is saved as .csv ASCII text format. The file names for each instrument is described separately for each instrument. The following convention is used: YYYY stands for the year, MM for the month, and DD for the day, all in numerals and with zero padding.

Included in the data set is the automatic weather system (AWS) data from the station. The data is in the aws_PaCE2022.zip file and the file names inside the zip archive are named FMI.AWS.a1.YYYYMMDD.csv. The files comprise 11 columns: datetime, Temp 570m (C), Dew point temp (C), Humidity 570m (%), Pressure (hPa), Wind speed (m/s), Wind dir (deg), Sun rad 1 (W/m2), Sun rad 2 (umol/s/m2), FD12P visibility (m), and Rain intensity (mm/h). The datetime columns shows the end time of the sampling period in as YYYY-MM-DD HH:MM:SS. Temp 570m (C) is the ambient temperature at the station in °C, Dew point temp (C) is the ambient dew point temperature in °C, Pressure (hPa) is the ambient pressure in hPa, Wind speed

https://doi.org/10.5194/essd-2025-284
Preprint. Discussion started: 24 June 2025
© Author(s) 2025. CC BY 4.0 License.

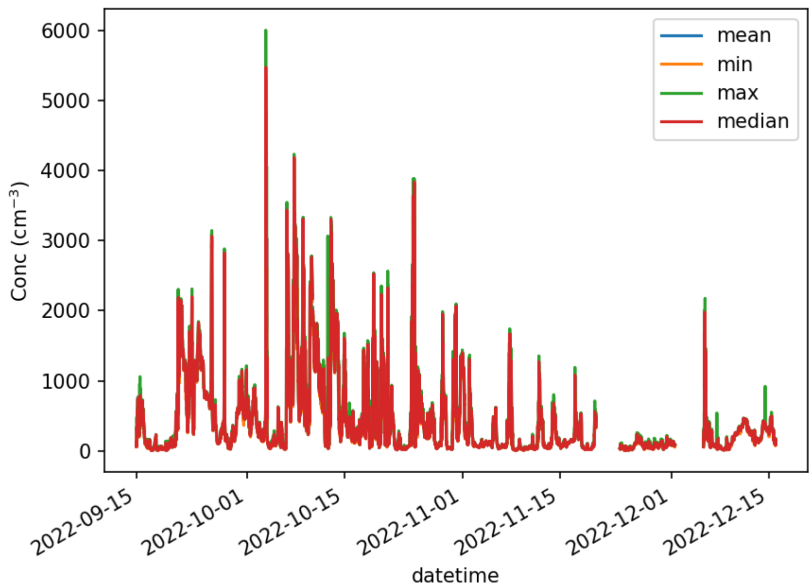

Figure 2. Total particle number concentration as measured by the CPC (TSI inc. model 3772). The native time resolution of the data is 1 s but the logging software saves the data as 5 min averages. The logging software saves the minimum, maximum, mean, and median concentration during the data collection. All those statistics are shown in the figure.

(m/s) is the wind speed in m/s, Wind dir is the horizontal wind direction in degrees. Sun rad 1 (W/m2) is the global solar radiation in Wm^{-2} and Sun rad 2 (umol/s/m2) is the photosynthetically active radiation in units of µmol m^{-2}s^{-1}), and FD12P visibility (m) is the horizontal visibility (m).

3.1 CPC

A critical orifice in the CPCs should keep the flow at a constant flow rate of 1 vlpm. The firmware of the instruments assumes this flow rate and calculates the concentration according to that, regardless of the actual flow rate. The correct concentration, after taking into account the measured flow rate through the CPC, is obtained by multiplying the measured concentration by the CPC with the calculated F_{flow} from Eq. 2. Ideally, the assumed and measured flow rate should be the same.

The measured concentration by the CPC also depends on the environmental conditions of the CPC, i.e., that it is working correctly. These include the temperature difference between the condenser and saturator (which is kept at 17 °C) and that the external vacuum is sufficient. The temperature difference is monitored directly by the instrument itself whereas the external vacuum is monitored through pressure difference sensors across a nozzle and the critical orifice of the instrument. All periods where either the temperature difference or the pressure difference has been out of bonds have been removed from the data.

https://doi.org/10.5194/essd-2025-284
Preprint. Discussion started: 24 June 2025
© Author(s) 2025. CC BY 4.0 License.

The CPC daily data files are in the cpc_pm25_PaCE2022.zip file as comma separated .csv files that are named FMI.CPC.b1.YYYYMMDD.csv. The files contain 7 columns: datetime, mean, min, max, median, in_cloud, RH. The datetime columns shows the end time of the sampling period in as YYYY-MM-DD HH:MM:SS. The mean, min max, and median columns show the statistic from the raw 1 s data in cm^{-3} in STP conditions. The in_cloud columns is either True or False and indicates if the station was inside a cloud or not. The RH(%) columns shows the RH(%) of the sample air in % the inlet. Removed or missing data are left empty; i.e. visible in the data as two subsequent commas.

The flow rate of the CPC was measured to be between 0.941 and 0.952 vlpm with an external flow meter. The flow rate should be 1.0 vlpm. The flow rate difference was compensated for using Eq. 2.

3.2 DMPS

The DMPS is connected to the $PM_{2.5}$ inlet and has a time resolution of 6.5 min. The size range of the DMPS is from 10 to 800 nm and is measured in 30 bins by stepping through different voltages of the DMA. The bins are evenly spaced on a logarithmic scale. The particle number concentration after the DMA is measured with a TSI Inc. model 3010 CPC (Mertes et al., 1995). The DMA has a total length of 28 cm and an outer diameter of 33 mm and an inner diameter of 25 mm. The sheath flow's temperature and pressure is measured by a TSI Inc. mass flow meter. The sheath flow RH and the sample air RH are measured with a Vaisala HMP110 sensors. Periods when the RH has been above 40% have been removed from the data.

The sheath flow is arranged in a closed-loop configuration and the flow rate is kept constant using a critical orifice. A membrane pump is used to circulate the sheath flow. The sheath flow is also dried by passing the sheath flow through a bottle of silica gel, which is routinely changed. The silica gel bottle also acts as a damper for the membrane pump which evens out flow fluctuations caused by the membrane pump.

The sheath (Q_{sh}) and excess (Q_{e}) flow rate of the DMA is 5 vlpm and the aerosol (Q_{a}) and sample (Q_{s}) flow rates are 1 vlpm. A Q_{sh} of 5 vlpm allows for detection of aerosol particles with an electrical mobility from 10 to 800 nm using a 12.5 kV high voltage supply. The Q_{a} to Q_{sh} ratio (β) is 1/5. The value β is a measure of how broad the transfer function without considering aerosol particle diffusion Flagan (1999). The transfer function essentially describes the size range and probability of particles that passes the DMA when a voltage is applied. In brief, the transfer function of the DMA also depends on particle size, the geometry of the DMA, and the flow rates at which the DMA is operated Zhang and Flagan (1996). These are all taken into account during the data inversion of the DMPS data to get the ambient PNSD.

The data inversion uses the bipolar charge distribution for differently sized and charged particles according to Wiedensohler (1988). The DMA transfer function, including the broadening of the transfer function due to Brownian motion, is described by Stolzenburg (1988). The detection efficiency of the CPC is taken into account and is based on the measured detection limit by the European Center for Aerosol Calibration and Characterization (ECAC). During the data inversion, diffusion losses in the DMA, drier, and the sampling lines are corrected for using the analytical formulas by Hinds (1999). The diffusion losses in the Hauke-type DMA can be corrected for using an equivalent pipe length of 4.6 m (Karlsson and Martinsson, 2003). The Nafion diffusion drier has an equivalent pipe length of 2.5 m (Dick et al., 1995). In addition, the pipe lengths connecting the DMA and

https://doi.org/10.5194/essd-2025-284
Preprint. Discussion started: 24 June 2025
© Author(s) 2025. CC BY 4.0 License.

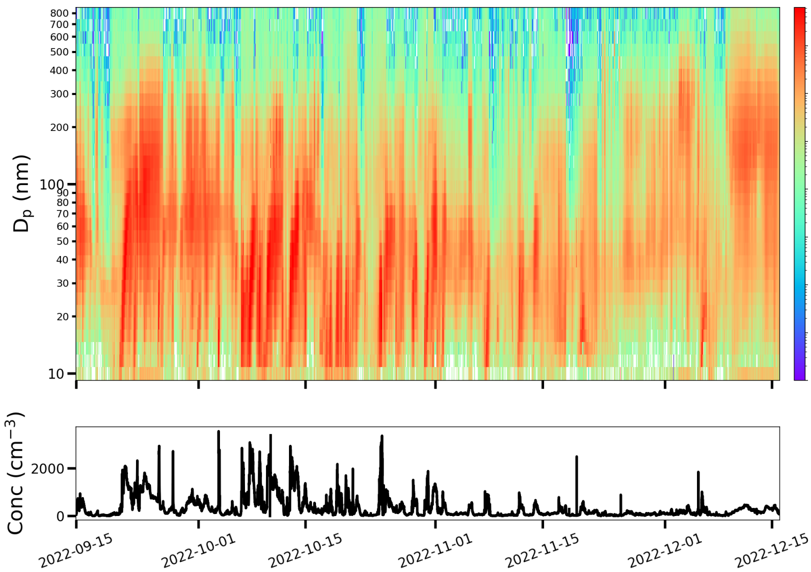

Figure 3. The figure shows the DMPS data in units of cm^{-3}. The upper panel shows the size distribution. The data displayed in the upper panel has been averaged to 1 h averages, for clarity. The native time resolution of the data is 6.5 minutes. The lower panel shows the PNC of the DMPS as calculated from the PNSD.

the driers are added to compensate for all diffusion losses in the sampling line. Since the diffusion losses are a function of pipe length and sample flow, the measured lengths and flows are used in the correction. The DMPS time series is shown in Fig. 3.

The DMPS daily data files are in the dmps_pm25_PaCE2022.zip file as comma separated .csv files that are named FMI.DMPS.c1.YYYYMMDD.csv. The files contain 37 columns. First column is datetime as YYYY-MM-DD HH:MM:SS, the following 30 columns are the bin centers of the dN/dlog(Dp) data in cm^{-3} and at STP conditions for the particle sizes of 10.0, 11.6, 13.5, 15.7, 18.3, 21.3, 24.8, 28.8, 33.5, 39.0, 45.3, 52.7, 61.3, 71.3, 82.9, 96.5, 112.2, 130.5, 151.8, 176.5, 205.3, 238.8, 277.8, 323.1, 375.8, 437.1, 508.4, 591.3, 687.8, and 800.0 nm. The diameters in the data files is in m. The rest of the columns are: total, pressure, temperature, RH, RH(%)_2.5, and in_cloud. The total columns is the PNC in STP calculated from the PNSD data in cm^{-3}, pressure is in kPa, temperature in K, RH is the sheath flow RH in % and RH(%)_2.5 is the sample inlet RH in %. The in_cloud columns is either True or False and indicates if the station was inside a cloud or not.

The flow rate of the DMPS's CPC was measured to be 0.989 and 0.999 vlpm. The sample aerosol flow rate into the DMA was measured to be between 0.80 and 0.847 vlpm. The flow rates were compensated for using Eq. 2. The sheath flow into the DMA was measured to be 5.06 vlpm and 5.11 whereas the DMA out flow was measured to be between 4.82 and 4.95 vlpm with an external bubble flow meter. Ideally, the CPC and the DMA-inlet flow rates should be the same. The small imbalance

https://doi.org/10.5194/essd-2025-284
Preprint. Discussion started: 24 June 2025
© Author(s) 2025. CC BY 4.0 License.

Open Access Earth System Science Data Discussions

was later found to be caused by a faulty connection in the suction side of the closed sheath flow loop arrangements of the DMA. The measured flow rates were used in the data inversion.

3.3 CCN

The CCNc total flow rate was 1.5 vlpm, consisting of 0.5 vlpm CCNc flow and 1 vlpm of CPC flow. A parallel CCNc-DMA setup flows were set to following, the sheath (Q_{sh}) and excess (Q_{e}) flow rates to 8 vlpm and the aerosol (Q_{a}) and sample (Q_{s}) flow rates of CPC to 1 vlpm. A sheath flow of 8 vlpm allows for detection of aerosol particles with an electrical mobility from 10 to 300 nm using a 12.5 kV high voltage supply. The CCNc-DMA size range of 10 - 300 nm was divided into 20 size bins using logarithmic scale (10, 11.96, 14.305, 17.109, 20.463, 24.475, 29.272, 35.011, 41.874, 50.083, 59.901, 71.643, 85.688, 102.485, 122.576, 146.605, 175.344, 209.718, 250.829 and 300 nm). The alternation between total and size resolved measurements was done every hour, resulting in 12 hours of total and 12 hours of size resolved CCN data per day. The CCNc was set to 6 supersaturations (SS) = 0.09, 0.1, 0.2, 0.3, 0.6 and 1.0. Each SS was kept for 10 minutes. The first SS was only used to stabilize temperature gradients after the highest SS=1.0. All data at SS=0.09 were discarded and not included in dataset due to temperature instability of the CCNc column. The CCNc SS calibration was done 4 times during the PaCE 2022 campaign, on August 31st, September 12th, October 3rd and November 14th, 2022. The SS calibration was done at 4 ΔT points with ΔT ranging from 3 to 17 K. The SS calibration average slope was 15.422 (std=0.991) and average intercept was 1.256 (std=0.230), at average pressure of 94.688 (std=0.641) kPa.

Two kinds of CCNc datasets are provided, the total CCN and size resolved, respectively. The total CCN count dataset includes minute resolution data with following 17 columns: datetime (UTC), set supersaturation - SS, concentration at SS0.9, std(0.9), concentraion at SS0.1, std(0.1), concentration at SS0.2, std(0.2), concentration at SS0.3, std(0.3), concentration at SS0.6, std(0.6), concentration at SS1.0, std(1.0), total concentration - CN, std(CN) and activated fraction - Act.

The size resolved CCN dataset includes daily averaged size resolved data, this is due to very low aerosol concentrations of aerosol measured at Sammaltunturi station, the statistics on binned concentrations are usually very low. The size resolved dataset includes 13 columns: Date, size resolved diameter - Dp, concentration measured at SS0.1, SS0.2, SS0.3, SS0.6, SS1.0, total concentration measured at set Dp - CN, calculated activated fraction (CCN/CN) for SS 0.1 - Act(0.1), calculated activated fraction for SS 0.2 - Act(0.2), calculated activated fraction for SS 0.3 - Act(0.3), calculated activated fraction for SS 0.6 - Act(0.6) and calculated activated fraction for SS 1.0 Act(1.0).

Furthermore, the size-resolved activation fraction (CCN/CN) was fitted with sigmoid function to derive critical diameter D_{50}. By applying the CCNc-measured D_{50} into κ - Köhler relationship, the CCN-based hygroscopicity parameter κ can be obtained by matching the critical supersaturation, which is the maximum supersaturation on the Köhler curve, (see e.g. Rose et al. (2008) and Petters and Kreidenweis (2007) for details on the method applied). The calculated hygroscopicity κ-values are provided in D50_kappa datasets. D50_kappa dataset contains 5 columns: date, supersaturation - SS, critical diameter in [nm] - D_c [nm], standard error of the fit - std_error, and resulting κ-values - kappa.

https://doi.org/10.5194/essd-2025-284
Preprint. Discussion started: 24 June 2025
© Author(s) 2025. CC BY 4.0 License.

3.4 APS

APS measures air sampled through the total inlet and the sample air dried with a Naphion drier. The total flow of the APS is 5 lpm: the sheath flow is 4 lpm and the sample flow is 1 lpm. During the PACE 2022 campaign, the APS at Pallas was changed due to malfunction in the middle of the measurement period.

The counts of the APS for each size bin (53 bins) were converted to particle size distribution as $\mathrm{d}N(\mathrm{dlog}D_\mathrm{p}^{-1})$ in the units of cm^{-3}. The conversion was done by dividing the counts in each size bin with the sample volume and the width of the size bin $(\mathrm{dlog}D_\mathrm{p})^{-1}$.

Time series of the measured size distribution and the total number of coarse mode particles are presented in Fig. 4. A two weeks long gap in October 2022 was due to instrument malfunctioning as the laser of the instrument stopped working. The broken APS was replaced with another one in November 2022.

The APS daily data files are in the aps_tot_PaCE2022.zip file as comma separated .csv files that are named FMI.APS.b1.YYYYMMDD.csv. The files contain 57 columns. First column is datetime as YYYY-MM-DD HH:MM:SS. The second columns is the total PNC as measured by the APS in cm^{-3}. The following 53 columns are the bin centers of the dN/dlog(Dp) data in cm^{-3} and at STP conditions for the particle sizes of dp_487, dp_523, dp_562, dp_604, dp_649, dp_698, dp_750, dp_806, dp_866, dp_931, dp_1000, dp_1075, dp_1155, dp_1241, dp_1334, dp_1433, dp_1540, dp_1655, dp_1778, dp_1911, dp_2054, dp_2207, dp_2371, dp_2548, dp_2738, dp_2943, dp_3162, dp_3398, dp_3652, dp_3924, dp_4217, dp_4532, dp_4870, dp_5233, dp_5623, dp_6043, dp_6494, dp_6978, dp_7499, dp_8058, dp_8660, dp_9306, dp_10000, dp_10746, dp_11548, dp_12409, dp_13335, dp_14330, dp_15399, dp_16548, dp_17783, dp_19110, and dp_20535. The particle size after "dp_" is in nm. The rest of the columns are: RH(%)_tot and in_cloud. RH(%)_tot is the sample inlet RH in %. The in_cloud columns is either True or False and indicates if the station was inside a cloud or not.

3.5 Nephelometer

The integrating nephelometer at Pallas is a TSI Inc. model 3563 Nephelometer (Anderson et al., 1996). TSI 3563 measures σ_sp and σ_bsp at 450, 550, and 700 nm wavelengths Anderson and Ogren (1998). The instrument samples through the total inlet and it was deployed at the site in 2001. The measurement resolution of the integrating nephelometer at Pallas is five minutes. The instrument is configured to measure particle-free air for five minutes every hour, which becomes the zero baseline for the instrument for the subsequent measurements.

Based on the stability of the regularly retrieved calibration parameters and the hourly measurements with filtered air, the general condition of the instrument was stable over the measurement period. The RH in the instrument was well below the recommended 40% for most of the the measurement period.

To correct for the not-detected scattering at the near forward and backward scattering angles (the angular measurement range for the TSI 3563 is 7-170°), the data are corrected with the truncation correction according to Anderson and Ogren (1998). Because the truncation correction depends on the particle size distribution, they recommend to apply the correction as a function of scattering Ångström exponent (α_sp, Ångström (1929)) that describes the wavelength dependency of σ_sp and

https://doi.org/10.5194/essd-2025-284
Preprint. Discussion started: 24 June 2025
© Author(s) 2025. CC BY 4.0 License.

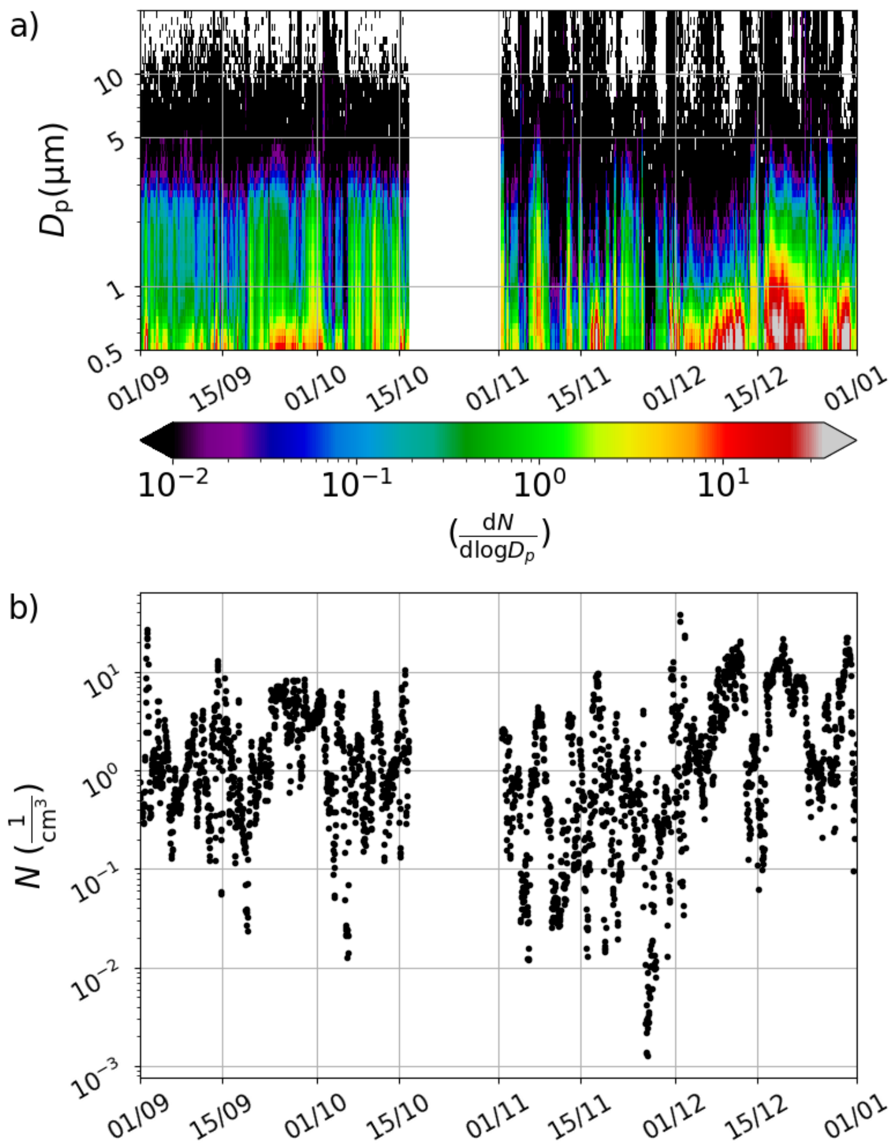

Figure 4. Time series of the APS measurements: a) aerosol size distribution for the diameter (D_p range 0.5 - 20 µm and b) total number concentration (N) of the aerosol particles in the coarse mode size range (here 0.5 - 20 µm).

indicates the variations in the volume mean diameter of the particles. As the integrating nephelometer is installed after the total inlet, we used the *No cut* -values given in Table 4 in Anderson and Ogren (1998). With the low concentrations at Pallas, the α_sp can be very noisy with high time resolution data; e.g. 5 min. Therefore, to get better statistics for deriving the α_sp, only the wavelength pair of 450 and 700 nm was used, instead of deriving the α_sp separate for wavelength ranges of 450-550 nm

https://doi.org/10.5194/essd-2025-284
Preprint. Discussion started: 24 June 2025
© Author(s) 2025. CC BY 4.0 License.

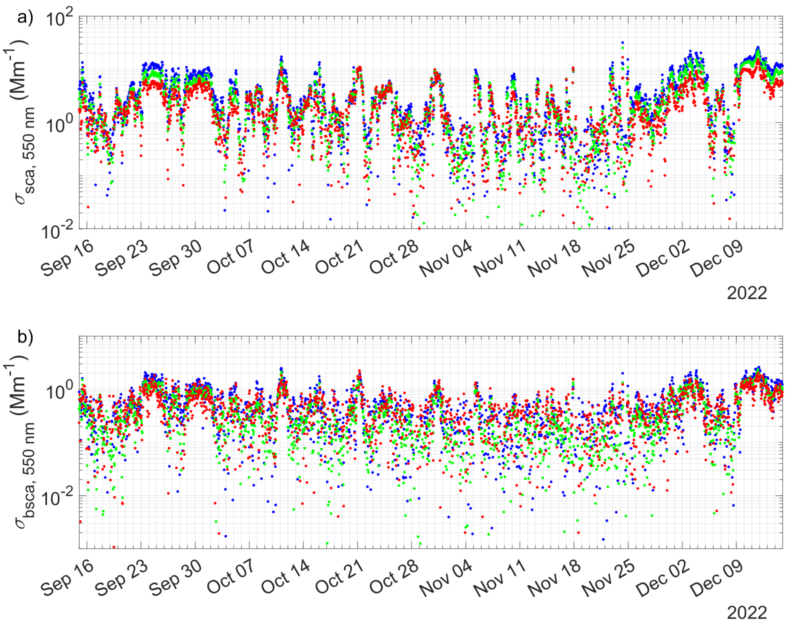

Figure 5. Time series of a) the total scattering and b) backscattering coefficients (σ_{sp} and σ_{bsp}, respectively). The σ_{sca} and σ_{bsp} are shown for each measured wavelength (450, 550, and 700 nm).

and 550-700 nm. Also, to reduce the noise, the α_{sp} was derived from 1 hour running mean values of $\sigma_{\mathrm{sp,450nm}}$ and $\sigma_{\mathrm{sp,700nm}}$ instead of using the native 5 min time resolution.

The Nephelometer daily data files are in the nephelometer_tot_PaCE2022.zip file as comma separated .csv files that are named FMI.NEPH.b1.YYYYMMDD.csv. The files contain the following 9 columns: datetime, RH(%), sca450(Mm-1), sca550(Mm-1), sca700(Mm-1), bsca450(Mm-1), bsca550(Mm-1), bsca700(Mm-1), and in_cloud. The datetime columns is in the form YYYYMMDDHHMMSS. RH(%) is in %. The columns sca450(Mm-1), sca550(Mm-1), sca700(Mm-1) are σ_{sp} in units of Mm^{-1} for the wavelength, 450, 550, and 700 nm, respectively. Similarly, the columns bsca450(Mm-1), bsca550(Mm-1), bsca700(Mm-1) are σ_{bsp} in units of Mm^{-1} for the wavelength, 450, 550, and 700 nm.

During the measurement period 15 September to 15 December 2022, the instrument was calibrated with CO_2 once. In October 2023, the red wavelength (700 nm) was found to be a bit noisy during an inter-comparison workshop at ECAC. The nephelometer has passed the inter-comparison workshops in 2017 and 2019.

3.6 Filter-based absorption photometers (MAAP and AE-33)

Both the MAAP and the AE-33 are filter-based absorption photometers that report the measured σ_{ap} as eBC mass concentrations. Since the data post-processing for both absorption photometers is similar, the data post-processing is described in the same subsection. The eBC mass concentration can be converted back to σ_{ap} as using the equation

$$\sigma_{\lambda,\mathrm{ap}} = MAC_{\lambda}\; eBC_{\lambda} \tag{3}$$

where λ is the wavelength of light and MAC is the assumed mass absorption cross-section (in $\mathrm{m^2g^{-1}}$) of the aerosol.

The MAAP is a single wavelength instrument measuring at 637 nm, whereas the AE-33 is a 7-wavelength instrument measuring at 370, 470, 520, 590, 660, 880, 950 nm. Data from both instruments can be converted back to σ_{ap} using Eq. 3. The MAC value for the MAAP is 6.6 $\mathrm{m^2g^{-1}}$ at 670 nm wavelength. The manufacturer initially reported that the λ of the light source was 670 nm but was later measured to be 637 nm (Müller et al., 2011). Because of this, an additional correction factor of 1.05 is needed to get σ_{ap} at 637 nm and would correspond to a MAC of 6.93 $\mathrm{m^2g^{-1}}$ at 637 nm (Müller et al., 2011). The MAC values for the AE-33 are 18.47, 14.54, 13.14, 11.58, 10.35, 7.77, 7.19 $\mathrm{m^2g^{-1}}$ for the 7 different wavelengths (370, 470, 520, 590, 660, 880, 950 nm).

In filter-based absorption photometers, the σ_{ap} value is calculated from the change in filter properties and from the amount of air drawn through the filter during which that change was observed; i.e. the sampling interval. The measured σ_{ap} value is therefore directly proportional to the flow rate through the filter. Thus, the σ_{ap} values have been corrected using F_{flow} from Eq. 2 as described in (Bond et al., 1999). Routinely measured sample flow rates at the instrument's inlet are used to correct the reported mass concentrations of eBC using Eq. 2. For the AE-33, F_{flow} was between 0.99 and 1.00 during the year 2022. For the MAAP, F_{flow} was in the range of 0.97 to 1.07 during 2022.

Before the filter tape gets too laden with aerosol particles, the filter tape is advanced so that a new filter spot is used. This makes both the MAAP and AE-33 instruments ideal for long-term monitoring and unattended use. The MAAP changes the filter spot when the filter transmission has reduced from 100% to 20% whereas the AE-33 will invoke a filter change when the ATN value (see Eq. 1) of one channel has reached 120.

The native time resolution of the AE-33 is 1 min. The data is shown in Fig. 6 in σ_{ap}.

The Aethalometer AE-33 daily data files are in the ae33_tot_PaCE2022.zip file as comma separated .csv files that are named FMI.AE33.b1.YYYYMMDD.csv. The files contain the following 10 columns: datetime, abs370, abs470, abs525, abs590, abs590, abs660, abs880, abs950, in_cloud, and RH(%)_tot. The datetime columns is in the form YYYY-MM-DD HH:MM:SS. RH(%)_tot is the RH of the total inlet in %. The columns abs370, abs470, abs525, abs590, abs590, abs660, abs880, abs950 contain σ_{ap} in units of $\mathrm{Mm^{-1}}$ for the wavelength, 370, 470, 525, 590, 660, 880, 950 nm, respectively. The in_cloud columns is either True or False and indicates if the station was inside a cloud or not.

The MAAP daily data files are in the maap_pm25_PaCE2022.zip file as comma separated .csv files that are named FMI.MAAP.b1.YYYYMMDD.csv. The files contain the following 4 columns: datetime, abs637, in_cloud, and RH(%)_2.5. The datetime columns is in the form YYYY-MM-DD HH:MM:SS. RH(%)_2.5 is the RH of the total PM2.5 inlet in %. The column abs637 contain σ_{ap} in units of $\mathrm{Mm^{-1}}$ for the wavelength 637 nm. The in_cloud columns is either True or False and indicates if the station was inside a cloud or not.

https://doi.org/10.5194/essd-2025-284
Preprint. Discussion started: 24 June 2025
© Author(s) 2025. CC BY 4.0 License.

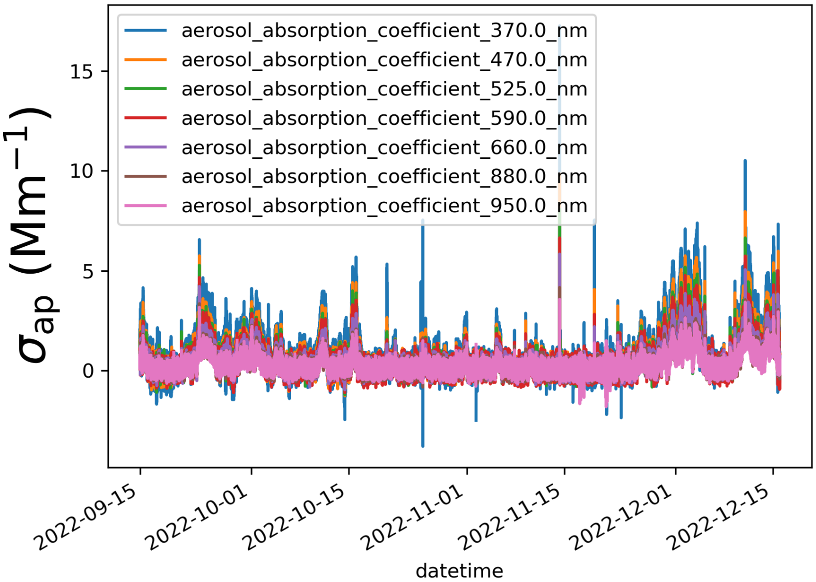

Figure 6. Time series of light absorption coefficients (σ_{ap}) at 370 and 880 nm wavelengths during the campaign from the AE-33.

4 Summary

The measurements described here were a part of the Pallas Cloud Experiment 2022 (PaCE 2022). The PaCE 2022 campaign took place between 15 September 2022 and 15 December 2022. The measurement principles and theory of operation is described in detail in Sect. 2 along with additional information about the inlets and the measurement site in general. The data processing for the final data is described in Sect. 3. This work describes how the measurements were conducted and how the data was processed to achieve the final data that is presented in the data set.

The instruments and measurements described here are, however, part of the routine measurements conducted at the Sammaltunturi measurement station in Pallas and are conducted all year around, except for the CCN instrument.

5 Data availability

The data set is published by Backman et al. (2025). The dataset was published at the Zenodo Open Science data archive, under a dedicated community Pallas Cloud Experiment – PaCE2022 (https://zenodo.org/communities/pace2022/, last access: 7 May 2025)

https://doi.org/10.5194/essd-2025-284
Preprint. Discussion started: 24 June 2025
© Author(s) 2025. CC BY 4.0 License.

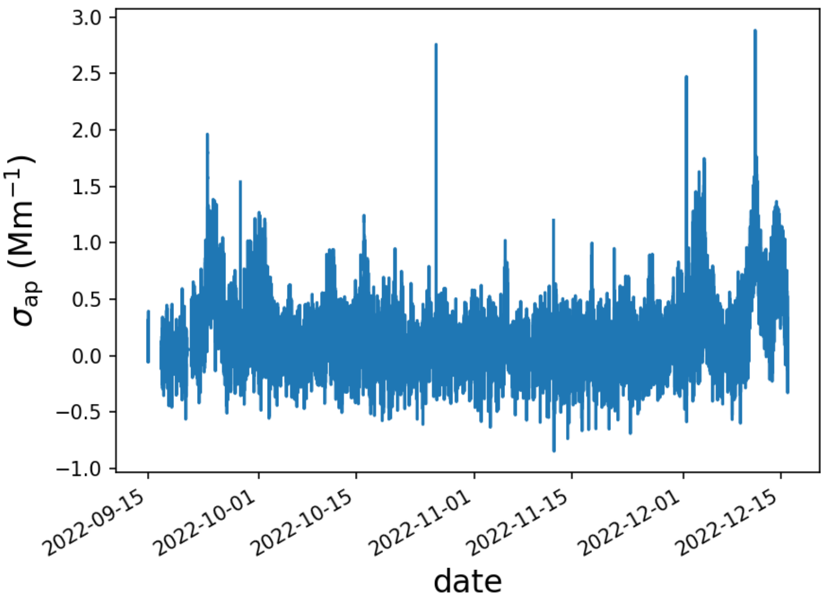

Figure 7. Time series of light absorption coefficients (σ_{ap}) at 637 nm wavelengths during the campaign from the MAAP.

Financial support. This work was supported by ACTRIS IMP GA 871115, ACTRIS-Finland funding through the Ministry of Transport and Communications, the Atmosphere and Climate Competence Center Flagship funding by the Research Council of Finland (Grants 337552). This project has also received funding from the European Union, H2020 research and innovation program (ACTRIS-IMP, the European Research Infrastructure for the observation of Aerosol, Clouds, and Trace gases, Grant 871115).

Author contributions. JB, KL and DB did most of the writing and data processing. HS took care of the instruments and routine maintenance at the site. All authors contributed to the editing of the manuscript.

Competing interests. The authors declare that they have no competing interests.

https://doi.org/10.5194/essd-2025-284
Preprint. Discussion started: 24 June 2025
© Author(s) 2025. CC BY 4.0 License.

References

Albrecht, B. A.: Aerosols, Cloud Microphysics, and Fractional Cloudiness, Science, 245, 1227–1230, https://doi.org/10.1126/science.245.4923.1227, 1989.

Anderson, T., Covert, D., Marshall, S., Laucks, M., Charlson, R., Waggoner, A., Ogren, J., Caldow, R., Holm, R., Quant, F., Sem, G., Wiedensohler, A., Ahlquist, N., and Bates, T.: Performance Characteristics of a High-Sensitivity, Three-Wavelength, Total Scatter/Backscatter Nephelometer, Journal of Atmospheric and Oceanic Technology, 13, 967 – 986, https://doi.org/10.1175/1520-0426(1996)013<0967:PCOAHS>2.0.CO;2, 1996.

Anderson, T. L. and Ogren, J. A.: Determining Aerosol Radiative Properties Using the TSI 3563 Integrating Nephelometer, Aerosol Science and Technology, 29, 57–69, https://doi.org/10.1080/02786829808965551, 1998.

Anttila, T., Brus, D., Jaatinen, A., Hyvärinen, A.-P., Kivekäs, N., Romakkaniemi, S., Komppula, M., and Lihavainen, H.: Relationships between particles, cloud condensation nuclei and cloud droplet activation during the third Pallas Cloud Experiment, Atmospheric Chemistry and Physics, 12, 11 435–11 450, https://doi.org/10.5194/acp-12-11435-2012, 2012.

Asmi, E., Kivekäs, N., Kerminen, V.-M., Komppula, M., Hyvärinen, A.-P., Hatakka, J., Viisanen, Y., and Lihavainen, H.: Secondary new particle formation in Northern Finland Pallas site between the years 2000 and 2010, Atmospheric Chemistry and Physics, 11, 12 959–12 972, https://doi.org/10.5194/acp-11-12959-2011, 2011.

B. T. Chen, Y. S. C. and Yeh, H. C.: Performance of a TSI Aerodynamic Particle Sizer, Aerosol Science and Technology, 4, 89–97, https://doi.org/10.1080/02786828508959041, 1985.

Backman, J., Luoma, K., Servomaa, H., Vakkari, V., and Brus, D.: In-situ aerosol measurements at the Arctic Sammaltunturi measurement station during the Pallas Cloud Experiment 2022 [dataset], https://doi.org/10.5281/ZENODO.14900651, 2025.

Bond, T. C., Anderson, T. L., and Campbell, D.: Calibration and Intercomparison of Filter-Based Measurements of Visible Light Absorption by Aerosols, Aerosol Science and Technology, 30, 582–600, https://doi.org/10.1080/027868299304435, 1999.

Brus, D., Doulgeris, K., Bagheri, G., Bodenschatz, E., Chávez-Medina, V., Schlenczek, O., Khodamodari, H., Pohorsky, R., Schmale, J., Lonardi, M., Favre, L., Böhmländer, A., Möhler, O., Lacher, L., Girdwood, J., Gratzl, J., Grothe, H., Kaikkonen, V., Molkoselkä, E., Mäkynen, A., O'Connor, E., Leskinen, N., Tukiainen, S., Le, V., Backman, J., Luoma, K., Servomaa, H., and Asmi, E.: Data generated during the Pallas Cloud Experiment 2022 campaign: an introduction and overview, submitted to Earth System Science Data, 2025.

Dagan, G., Yeheskel, N., and Williams, A. I. L.: Radiative forcing from aerosol–cloud interactions enhanced by large-scale circulation adjustments, Nature Geoscience, 16, 1092–1098, https://doi.org/10.1038/s41561-023-01319-8, 2023.

Dick, W., Huang, P., and McMurry, P.: Characterization of 0.02 to 1.0 μm particle losses in Perma Pure dryers: dependency on size, charge and relative humidity, PTL Publication No. 936: Particle Technologogy Laboratory, Department of Mechanical Engineering, University of Minnesota, Minneapolis, MN, 55455, 1–15, 1995.

Doulgeris, K.-M., Komppula, M., Romakkaniemi, S., Hyvärinen, A.-P., Kerminen, V.-M., and Brus, D.: In situ cloud ground-based measurements in the Finnish sub-Arctic: intercomparison of three cloud spectrometer setups, Atmospheric Measurement Techniques, 13, 5129–5147, https://doi.org/10.5194/amt-13-5129-2020, 2020.

Doulgeris, K. M., Vakkari, V., O'Connor, E. J., Kerminen, V.-M., Lihavainen, H., and Brus, D.: Influence of air mass origin on microphysical properties of low-level clouds in a subarctic environment, Atmospheric Chemistry and Physics, 23, 2483–2498, https://doi.org/10.5194/acp-23-2483-2023, 2023.

© Author(s) 2025. CC BY 4.0 License.

Drinovec, L., Močnik, G., Zotter, P., Prévôt, A. S. H., Ruckstuhl, C., Coz, E., Rupakheti, M., Sciare, J., Müller, T., Wiedensohler, A., and Hansen, A. D. A.: The "dual-spot" Aethalometer: an improved measurement of aerosol black carbon with real-time loading compensation, Atmospheric Measurement Techniques, 8, 1965–1979, https://doi.org/10.5194/amt-8-1965-2015, 2015.

Dusek, U., Frank, G. P., Hildebrandt, L., Curtius, J., Schneider, J., Walter, S., Chand, D., Drewnick, F., Hings, S., Jung, D., Borrmann, S., and Andreae, M. O.: Size Matters More Than Chemistry for Cloud-Nucleating Ability of Aerosol Particles, Science, 312, 1375–1378, https://doi.org/10.1126/science.1125261, 2006.

Filioglou, M., Nikandrova, A., Niemelä, S., Baars, H., Mielonen, T., Leskinen, A., Brus, D., Romakkaniemi, S., Giannakaki, E., and Komppula, M.: Profiling water vapor mixing ratios in Finland by means of a Raman lidar, a satellite and a model, Atmospheric Measurement Techniques, 10, 4303–4316, https://doi.org/10.5194/amt-10-4303-2017, 2017.

Flagan, R. C.: On Differential Mobility Analyzer Resolution, Aerosol Science and Technology, 30, 556–570, https://doi.org/10.1080/027868299304417, 1999.

Gérard, V., Noziere, B., Fine, L., Ferronato, C., Singh, D. K., Frossard, A. A., Cohen, R. C., Asmi, E., Lihavainen, H., Kivekäs, N., Aurela, M., Brus, D., Frka, S., and Cvitešić Kušan, A.: Concentrations and Adsorption Isotherms for Amphiphilic Surfactants in PM1 Aerosols from Different Regions of Europe, Environmental Science & Technology, 53, 12 379–12 388, https://doi.org/10.1021/acs.est.9b03386, 2019.

Hatakka, J., Aalto, T., Aaltonen, V., Aurela, M., Hakola, H., Komppula, M., Laurila, T., Lihavainen, H., Paatero, J., Salminen, K., and Viisanen, Y.: Overview of the atmospheric research activities and results at Pallas GAW station, Boreal Env. Res., 8, 365–383, https://www.borenv.net/BER/archive/pdfs/ber8/ber8-365.pdf, 2003.

Haywood, J. M. and Shine, K. P.: The effect of anthropogenic sulfate and soot aerosol on the clear sky planetary radiation budget, Geophysical Research Letters, 22, 603–606, https://doi.org/10.1029/95gl00075, 1995.

Heintzenberg, J. and Charlson, R. J.: Design and Applications of the Integrating Nephelometer: A Review, Journal of Atmospheric and Oceanic Technology, 13, 987–1000, https://doi.org/10.1175/1520-0426(1996)013<0987:daaoti>2.0.co;2, 1996.

Hermann, M., Wehner, B., Bischof, O., Han, H.-S., Krinke, T., Liu, W., Zerrath, A., and Wiedensohler, A.: Particle counting efficiencies of new TSI condensation particle counters, Journal of Aerosol Science, 38, 674–682, https://doi.org/10.1016/j.jaerosci.2007.05.001, 2007.

Hinds, W.: Aerosol Technology, Properties, Behaviour, and Measurement of Airborne Particles, John Wiley & Sons Inc., 1999.

IPCC: The Earth's Energy Budget, Climate Feedbacks and Climate Sensitivity, p. 923–1054, Cambridge University Press, 2023.

Karlsson, M. N. and Martinsson, B. G.: Methods to measure and predict the transfer function size dependence of individual DMAs, Journal of Aerosol Science, 34, 603–625, https://doi.org/10.1016/s0021-8502(03)00020-x, 2003.

Kivekäs, N., Kerminen, V.-M., Raatikainen, T., Vaattovaara, P., Laaksonen, A., and Lihavainen, H.: Physical and chemical characteristics of aerosol particles and cloud-droplet activation during the Second Pallas Cloud Experiment (Second PaCE), Boreal Env. Res., 14, 515–526, https://www.borenv.net/BER/archive/pdfs/ber14/ber14-515.pdf, 2009.

Knutson, E. and Whitby, K.: Aerosol classification by electric mobility: apparatus, theory, and applications, Journal of Aerosol Science, 6, 443–451, https://doi.org/10.1016/0021-8502(75)90060-9, 1975.

Komppula, M., Lihavainen, H., Kerminen, V., Kulmala, M., and Viisanen, Y.: Measurements of cloud droplet activation of aerosol particles at a clean subarctic background site, Journal of Geophysical Research: Atmospheres, 110, https://doi.org/10.1029/2004jd005200, 2005.

Lihavainen, H., Kerminen, V.-M., and Remer, L. A.: Aerosol-cloud interaction determined by both in situ and satellite data over a northern high-latitude site, Atmospheric Chemistry and Physics, 10, 10 987–10 995, https://doi.org/10.5194/acp-10-10987-2010, 2010.

https://doi.org/10.5194/essd-2025-284
Preprint. Discussion started: 24 June 2025
© Author(s) 2025. CC BY 4.0 License.

McMurry, P. H.: The History of Condensation Nucleus Counters, Aerosol Science and Technology, 33, 297–322, https://doi.org/10.1080/02786820050121512, 2000.

Mertes, S., Schröder, F., and Wiedensohler, A.: The Particle Detection Efficiency Curve of the TSI-3010 CPC as a Function of the Temperature Difference between Saturator and Condenser, Aerosol Science and Technology, 23, 257–261, https://doi.org/10.1080/02786829508965310, 1995.

Morrison, H., van Lier-Walqui, M., Fridlind, A. M., Grabowski, W. W., Harrington, J. Y., Hoose, C., Korolev, A., Kumjian, M. R., Milbrandt, J., Pawlowska, H., Posselt, D. J., Prat, O. P., Reimel, K. J., Shima, S.-I., van Diedenhoven, B., and L., X.: Confronting the challenge of modeling cloud and precipitation microphysics., Journal of Advances in Modeling Earth Systems, 11, https://doi.org/https://doi.org/10.1029/2019MS001689, 2022.

Müller, T., Henzing, J. S., de Leeuw, G., Wiedensohler, A., Alastuey, A., Angelov, H., Bizjak, M., Collaud Coen, M., Engström, J. E., Gruening, C., Hillamo, R., Hoffer, A., Imre, K., Ivanow, P., Jennings, G., Sun, J. Y., Kalivitis, N., Karlsson, H., Komppula, M., Laj, P., Li, S.-M., Lunder, C., Marinoni, A., Martins dos Santos, S., Moerman, M., Nowak, A., Ogren, J. A., Petzold, A., Pichon, J. M., Rodriquez, S., Sharma, S., Sheridan, P. J., Teinilä, K., Tuch, T., Viana, M., Virkkula, A., Weingartner, E., Wilhelm, R., and Wang, Y. Q.: Characterization and intercomparison of aerosol absorption photometers: result of two intercomparison workshops, Atmospheric Measurement Techniques, 4, 245–268, https://doi.org/10.5194/amt-4-245-2011, 2011.

Petters, M. D. and Kreidenweis, S. M.: A single parameter representation of hygroscopic growth and cloud condensation nucleus activity, Atmospheric Chemistry and Physics, 7, 1961–1971, https://doi.org/https://doi.org/10.5194/acp-7-1961-2007, 2007.

Petzold, A. and Schönlinner, M.: Multi-angle absorption photometry—a new method for the measurement of aerosol light absorption and atmospheric black carbon, Journal of Aerosol Science, 35, 421–441, https://doi.org/https://doi.org/10.1016/j.jaerosci.2003.09.005, 2004.

Petzold, A., Schloesser, H., Sheridan, P. J., Arnott, W. P., Ogren, J. A., and Virkkula, A.: Evaluation of Multiangle Absorption Photometry for Measuring Aerosol Light Absorption, Aerosol Science and Technology, 39, 40–51, https://doi.org/10.1080/027868290901945, 2005.

Petzold, A., Ogren, J. A., Fiebig, M., Laj, P., Li, S.-M., Baltensperger, U., Holzer-Popp, T., Kinne, S., Pappalardo, G., Sugimoto, N., Wehrli, C., Wiedensohler, A., and Zhang, X.-Y.: Recommendations for reporting black carbon measurements, Atmospheric Chemistry and Physics, 13, 8365–8379, https://doi.org/10.5194/acp-13-8365-2013, 2013.

Pfeifer, S., Müller, T., Weinhold, K., Zikova, N., Martins dos Santos, S., Marinoni, A., Bischof, O. F., Kykal, C., Ries, L., Meinhardt, F., Aalto, P., Mihalopoulos, N., and Wiedensohler, A.: Intercomparison of 15 aerodynamic particle size spectrometers (APS 3321): uncertainties in particle sizing and number size distribution, Atmospheric Measurement Techniques, 9, 1545–1551, https://doi.org/10.5194/amt-9-1545-2016, 2016.

Rantanen, M., Karpechko, A. Y., Lipponen, A., Nordling, K., Hyvärinen, O., Ruosteenoja, K., Vihma, T., and Laaksonen, A.: The Arctic has warmed nearly four times faster than the globe since 1979, Communications Earth Environment, 3, https://doi.org/10.1038/s43247-022-00498-3, 2022.

Rose, D., Gunthe, S., Mikhailov, E., Frank, G. P., Dusek, U., Andreae, M. O., and Pöschl, U.: Calibration and measurement uncertainties of a continuous-flow cloud condensation nuclei counter (DMT-CCNC): CCN activation of ammonium sulfate and sodium chloride aerosol particles in theory and experiment, Atmospheric Chemistry and Physics, 8, 1153–1179, https://doi.org/https://doi.org/10.5194/acp-8-1153-2008, 2008.

Schmale, J., Zieger, P., and Ekman, A.: Aerosols in current and future Arctic climate., Nature Climate Change, 11, 95–105, https://doi.org/https://doi.org/10.1038/s41558-020-00969-5, 2021.

https://doi.org/10.5194/essd-2025-284
Preprint. Discussion started: 24 June 2025
© Author(s) 2025. CC BY 4.0 License.

Serreze, M. C., Barrett, A. P., Stroeve, J. C., Kindig, D. N., and Holland, M. M.: The emergence of surface-based Arctic amplification, The Cryosphere, 3, 11–19, https://doi.org/10.5194/tc-3-11-2009, 2009.

Stolzenburg, M. R.: An ultrafine aerosol size distribution measuring system, University of Minnesota, 1988.

Tuch, T., Weinhold, K., Merkel, M., Nowak, A., Klein, T., Quincey, P., Stolzenburg, M., and Wiedensohler, A.: Dependence of CPC cut-off diameter on particle morphology and other factors, Aerosol Science and Technology, 50, 331–338, https://doi.org/10.1080/02786826.2016.1152351, 2016.

Twomey, S.: Pollution and the planetary albedo, Atmospheric Environment (1967), 8, 1251–1256, https://doi.org/10.1016/0004-6981(74)90004-3, 1974.

Twomey, S.: The Influence of Pollution on the Shortwave Albedo of Clouds, Journal of the Atmospheric Sciences, 34, 1149–1152, https://doi.org/10.1175/1520-0469(1977)034<1149:tiopot>2.0.co;2, 1977.

Vasilatou, K., Wälchli, C., Iida, K., Horender, S., Tritscher, T., Hammer, T., Rissler, J., Gaie-Levrel, F., and Auderset, K.: Extending traceability in airborne particle size distribution measurements beyond 10 μm: Counting efficiency and unit-to-unit variability of four aerodynamic particle size spectrometers, Aerosol Science and Technology, 57, 24–34, https://doi.org/10.1080/02786826.2022.2139659, 2022.

Weingartner, E., Nyeki, S., and Baltensperger, U.: Seasonal and diurnal variation of aerosol size distributions ($10< D < 750$ nm) at a high-alpine site (Jungfraujoch 3580 m asl), Journal of Geophysical Research: Atmospheres, 104, 26 809–26 820, https://doi.org/10.1029/1999jd900170, 1999.

Wiedensohler, A.: An approximation of the bipolar charge distribution for particles in the submicron size range, Journal of Aerosol Science, 19, 387–389, https://doi.org/10.1016/0021-8502(88)90278-9, 1988.

Winklmayr, W., Reischl, G., Lindner, A., and Berner, A.: A new electromobility spectrometer for the measurement of aerosol size distributions in the size range from 1 to 1000 nm, Journal of Aerosol Science, 22, 289–296, https://doi.org/10.1016/s0021-8502(05)80007-2, 1991.

Zhang, S.-H. and Flagan, R. C.: Resolution of the radial differential mobility analyzer for ultrafine particles, Journal of Aerosol Science, 27, 1179–1200, https://doi.org/10.1016/0021-8502(96)00036-5, 1996.

Ångström, A.: On the Atmospheric Transmission of Sun Radiation and on Dust in the Air, Geografiska Annaler, 11, 156–166, http://www.jstor.org/stable/519399, 1929.